

THREE-DIMENSIONAL NUMERICAL SIMULATION OF ARC AND METAL TRANSPORT FOR STACKING DEPOSITION IN ARC WELDING BASED ADDITIVE MANUFACTURING

Xiangman Zhou*, Haiou Zhang*† and Guilan Wang**

* State Key Laboratory of Digital Manufacturing Equipment and Technology, Huazhong University of Science and Technology, Wuhan 430074, PR China

** State Key Laboratory of Materials Processing and Die & Mould Technology, Huazhong University of Science and Technology, Wuhan 430074, PR China

Abstract

The stacking deposition in arc welding based additive manufacturing (AWAM) results in complex surfaces of deposited layer. Therefore the electromagnetic force in molten pool, arc pressure, plasma shear stress and heat flux on molten pool surface are not the same as the conventional welding. A three-dimensional weak coupling modeling method has been developed to simulate the arc, molten pool dynamic and droplet impingement of stacking deposition. In the arc model, the molten pool is simplified to be solid state on the basis of experimentally observed result. The arc is simulated firstly, and then the electromagnetic force, arc pressure, plasma shear stress and heat flux are extracted and transmitted to metal transport model. The molten pool morphology of simulated result accords well with experimental result, which indicates that this weak coupling modeling method is capable of simulating the complex heat and mass transfer behaviors in AWAM.

Introduction

Additive manufacturing (AM) is characterized by fabricating a component through the deposition of materials layer-by-layer, which has gained worldwide popularity over the past few decades. Many AM techniques have been developed to fabricate metal components, such as selective laser melting (SLM) [1], selective laser sintering (SLS) [2], electron beam melting (EBM) [3] or electron beam freeform fabrication (EBF3) [4], and arc welding based additive manufacturing (AWAM) [5-9]. Compared with other AM techniques, the AWAM is an efficient and low-cost AM technology. The deposition rate of AWAM is about 50–130 g/min, and the energy efficiency can be as high as 90% [10], which are 13-25 times and 4.5-6 times than electron beam, respectively. Consequently, the AWAM is a promising option to conventional subtractive manufacturing for fabricating large aeronautical and naval components that feature high buy-to-fly ratio [9].

In AWAM, the gas metal arc welding (GMAW) or gas tungsten arc welding (GTAW) are usually employed as heat source, therefore the heat and mass transfer during the AWAM deposition are similar to the conventional arc welding process. Many works were devoted to study the arc welding by experimental way. Although experimental observations can provide some invaluable information, it is difficult to accurately measure arc parameters and reveal the underlying mechanisms during the arc welding process due to the extreme high temperature and high velocity. Therefore, numerical modeling has been broadly employed to understand the physical phenomena observed in the arc welding process. There are three types of mathematical model on arc welding simulation: arc model [11-14], metal transport model [15-20] and unified model [21-29], namely, the arc and metal are unified simulated in one model and the arc and metal are coupled at inner interface. The arc model and metal transport model can be collectively referred to as separated model. In these separated models, the heat and mass transfer between arc and workpiece are not considered.

The arc simulations are usually applied to study heat and mass transfer mechanism of high temperature arc. Xu ^[11] developed a three-dimensional mathematical model of arc in GTAW and presented a method to calculate 3D arc pressure, heat flux, and current density on the surface of the weld pool. Haidar ^[12] established an arc model to study the dynamic effects of metal vapor in gas metal arc welding. Recently, Ding ^[13] developed a three-dimensional mathematical model for describing arc plasma behavior in double-wire gas metal arc welding (DW-GMAW), and the effect of welding current on inclined angle, maximum temperature of arc plasma and heat flux on workpiece was investigated. Zhou ^[14] developed a three-dimensional numerical model of electric arc based on magnetic fluid dynamics for arc based additive forming process with pure argon shielding gas. The influences of surface topographies of deposited layer on the shape and state, heat and mass transfer of electric arc were investigated in details.

The metal transport model is usually developed to investigate the molten pool dynamic and droplet impingement in GMAW or molten pool dynamic in GTAW, in which the electromagnetic force and pressure of weld pool are usually calculated by empirical analytical formula ^[15-20]. Wu ^[15] presented a numerical simulation method for predicting the profile of the free surface deformation of fully-penetrated GTAW weld pool. The physical terms and the sign of Lagrange multiplier were used to derive the both front- and back-side deformation of weld pool surfaces equations. Chen et al. ^[16] developed a three-dimensional weld pool dynamics model for groove gas metal arc welding processes to study the influence of groove angle on welding of low carbon structural steel plates. The electromagnetic forces were calculated by empirical analytical formula, and the heat flux of arc was described as double elliptical distribution. Hu ^[17] and Rao ^[18] developed a three-dimensional transient model for weld pool dynamics and periodical impingement of filler droplets and investigated the effect on the formation of ripples in three-dimensional moving gas metal arc welding. The heat flux and arc pressure on surface of molten pool were considered to be a Gaussian distribution. Cho ^[19] developed a fluid dynamics simulation model for submerged arc welding process. The Abel inversion method with CCD camera images was adopted to develop the heat flux model of arc. Later, the modeling method of arc heat flux is performed to establish three-dimensional transient numerical simulation for second pass gas metal arc welding on V-groove in various welding positions ^[20].

In unified model, all the variables are solved in a unified solution domain, and the arc and metal are coupled at inner interface. Hu ^[21, 22] and Rao ^[23, 24] developed a two-dimensional unified comprehensive model to simulate the transport phenomena occurring during the gas metal arc welding process. And a harmonic mean of thermal conductivities was applied to process the heat conduction between the arc and the metal. Rao ^[23, 24] investigated the effect of the argon-helium mixtures on arc shape and metal transport phenomena. It found that the increase of helium content in the mixture shielding gas results in the change of arc shape and pressure distribution along the substrate surface as well as leads to the formation of larger droplets and the decrease of droplet detachment frequency. Murphy et al. ^[25, 26] presented a self-consistent three-dimensional model to investigate the heat and mass transport phenomena in gas metal arc welding by taking a special treatment of energy transfer between the workpiece and arc, namely the heating effect of the excited atoms that cause electrons to be emitted from the workpiece and accelerated by the sheath voltage was added to the energy conservation equation. Wang ^[27, 28] developed a unified model of coupled arc and weld pool for double electrodes GTAW. The weld pool dynamic was described by taking into account buoyance, electromagnetic force, surface tension and plasma drag force. And the influence of electrode separation on the flow and temperature fields of arc and weld pool were studied ^[28]. Recently, Jian et al. ^[29] developed a unified fluid flow and heat transfer model for stationary plasma arc welding. The VOF method was employed to track the keyhole boundary. And the whole evolution processes of keyhole formation were numerically simulated.

In AWAM, The stacking deposition are usually applied to fabricate thin-walled parts (as shown in Fig. 1), which will result in a unique surface topographies of deposited layer, as compared to the conventional arc welding. Consequently, the heat resource model, arc pressure model, and electromagnetic force model of

stacking deposition simulation are not identical with conventional welding and no longer symmetrical distribution. The unified model has advantages of solving the complex and asymmetric heat and mass transfer in arc welding, however the modeling and calculation processes are complex and time consuming [30]. Additionally, the physical mechanisms of coupling of arc and metal are not completely understood. Therefore, it is difficult to reproduce the unified model. As described in the previous section, the separated model has been widely applied in arc welding simulation. However, the electromagnetic force and pressure of weld pool are usually calculated by empirical analytical formula [15-20], or the parameters of heat flux model and arc pressure model are obtained through complex experiments [19, 20]. Therefore, the separated model is not a universal solution for arc and metal transport simulation in AWAM.

In present study, a three-dimensional weak coupling modeling method of arc and metal transport has been presented to simulate the arc, molten pool dynamic and droplet impingement in GMAW based additive manufacturing. The experimental observation shows that molten pool remains approximately constant surface shape during the AWAM deposition, therefore the arc model is developed based on the solid state molten pool firstly, and then the calculated results of electromagnetic force, arc pressure, plasma shear stress and heat flux are extracted and transmitted to metal transfer model to simulate the molten pool dynamic and droplet impingement. The volume of fluid (VOF) method is employed to track free surface of molten pool and droplet, and the continuum surface force (CSF) method is applied to transform all the surface forces on free surface as localized body forces. The CFD codes Fluent is used to solve these models, and the interpolation function of user-defined scalar (UDS) is applied to do the transmissions.

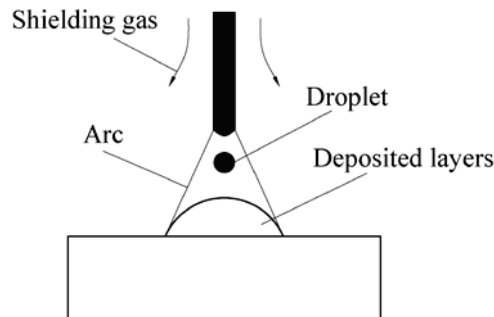


Fig. 1 A schematic representation of stacking deposition in AWAM

As shown in Fig. 2, a robot AWAM system with a high-speed camera system is established to carry out the deposition experiments and capture the molten pool and arc profile in this study.

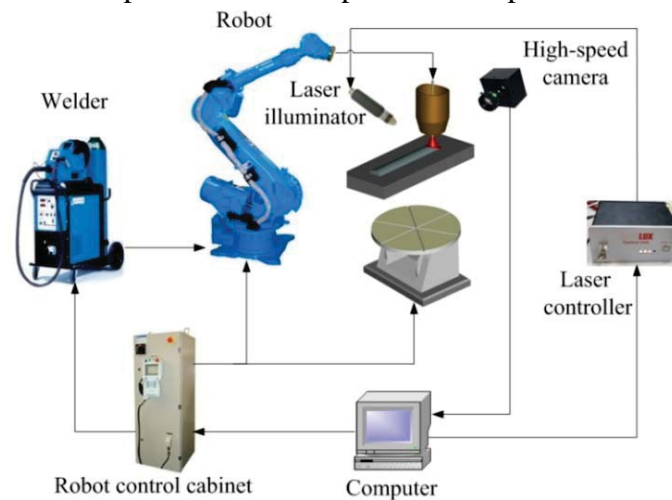


Fig. 2 The schematic diagram of robot based AWAM system

Mathematical models

1. Experimental basis

Fig. 3 is the images of weld bead and molten pool of second-layer deposition of single-pass thin-walled part at different instants, and Fig. 4 is the unfinished weld bead of second-layer deposition of the single-pass thin-walled part. The process parameters of present deposition are the same as simulation and given in Table 1. It can be seen from Fig. 3 that the weld bead and molten pool remain stable at different instants under the used process parameters. The Fig.4 shows that the finished deposited layers remain the same appearance. The above experimental observations indicate that the heat flux and forces of the molten pool remain stable substantially during the deposition. Therefore the molten pool is simplified to be solid state (as shown in Fig. 5) based on experimental observations in the arc model to simulate arc firstly, and then the heat flux and forces of the molten pool are extracted and transmitted to metal transport simulation.

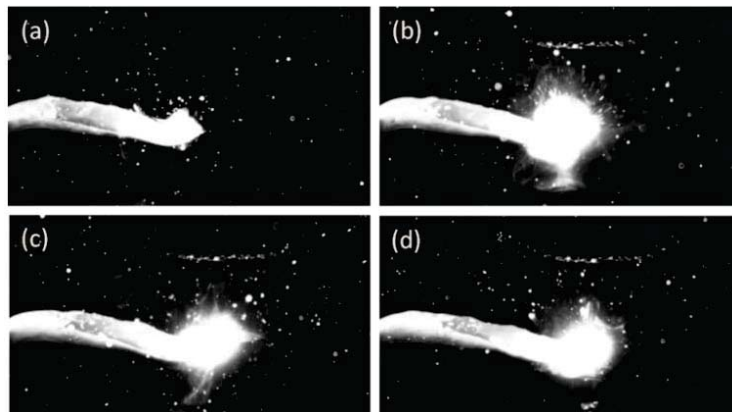


Fig. 3 The images of weld bead and molten pool of second-layer deposition of single-pass thin-walled part at different instants: (a) 0.6s; (b) 0.61s; (c) 0.62s; (d) 0.63s



Fig. 4 The unfinished weld bead of second-layer deposition of the single-pass thin-walled part: (a) top view; (b) front view.

Fig. 5 is schematic representation of arc model of second-layer deposition of single-pass thin-walled part. The molten pool is simplified to be solid state on the basis of above experimentally observed results. The distance between wire tip and substrate is 5 mm, the bead width is 10 mm and the bead height of second-layer is 6 mm under the used process parameters. The cross-sectional profile of single weld bead can be fitted by circular arc curve under the used process parameters^[31]. The second-layer begins to deposit when the center of first-layer is cooled to 180K. The deposition direction is the positive direction of the x-axis. To simplify the modeling, the top surface of first-layer is simplified to be a flat surface.

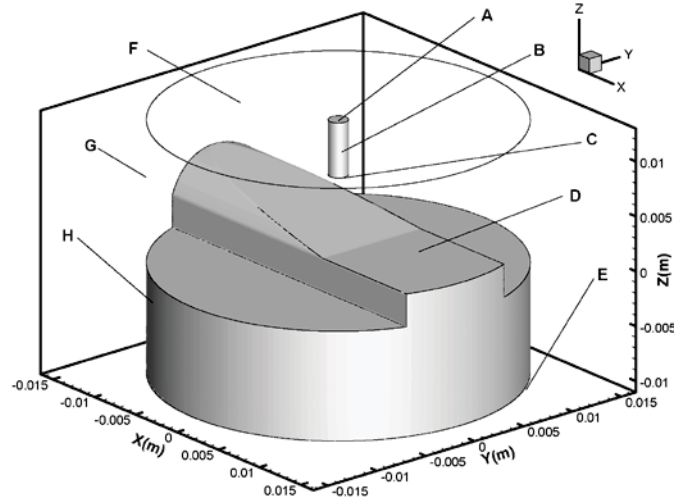


Fig. 5 The schematic representation of arc model

The schematic representation of metal transport model is illustrated in Fig. 6. Because the interpolation function of UDS is capable of adapting different grids under the same coordinate system, and to improve the computational efficiency, the domains of metal transport model are no longer the same with the arc model in present study.

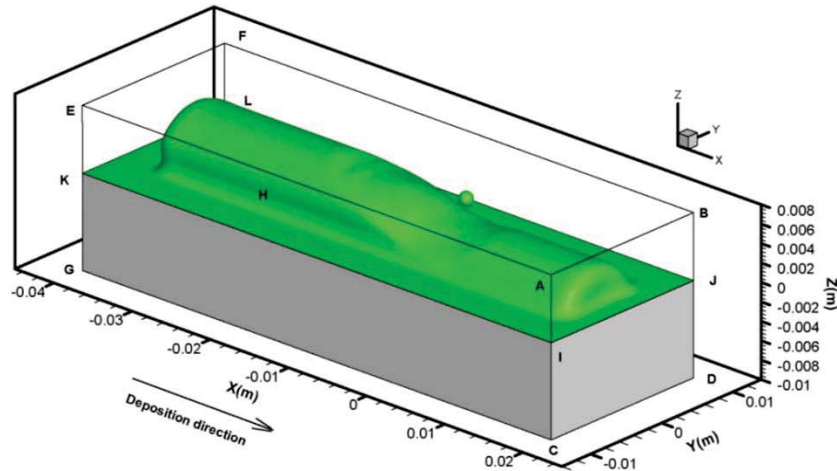


Fig. 6 The schematic representation of metal transport model

2. Governing equations

In the present numerical models, some simplifying assumptions made for the arc or metal transport simulation include:

(1) The arc and molten metal are considered to be laminar flow. The Reynolds number of arc and molten pool are about 670 and 2400, respectively. The transition from laminar flow to turbulent occurs at a Reynolds number of around is about 100000 for a free jet^[11] and 4000 for a normal flow. Therefore, the arc and molten metal can be modeled as laminar flow.

(2) The arc is in local thermodynamics equilibrium (LTE). This means electron and heavy particle temperatures are equal^[11, 32].

(3) The plasma arc is optically thin^[21, 23, 33, 34], which means the optical thin radiation loss per unit volume can be used in the arc model.

(4) The shielding gas is pure argon at 1atm, and the effect of metal vapor on plasma properties and presence of surrounding atmosphere are neglected [21, 23].

(5) The arc is considered as in steady state [11]. This means that the heat flux and forces of molten pool remain stable during the deposition.

With the above assumptions, the governing equations of heat and mass transfer for arc and metal transport of the second-layer deposition of single-pass thin-walled part are given below:

Mass continuity

$$\frac{\partial}{\partial t}(\rho) + \nabla \cdot (\rho \mathbf{V}) = S_{mass} \quad (1)$$

Momentum

$$\frac{\partial}{\partial t}(\rho \mathbf{V}) + \nabla \cdot (\rho \mathbf{V} \mathbf{V}) = -\nabla p + \nabla \cdot (\mu \nabla \mathbf{V}) + \rho g + S_M \quad (2)$$

Energy

$$\frac{\partial}{\partial t}(\rho h) + \nabla \cdot (\mathbf{V} \rho h) = \nabla \cdot \left(\frac{k}{c_p} \nabla h \right) + S_E \quad (3)$$

In the above equations, ρ is density, \mathbf{V} is velocity vector, p is pressure, and μ is viscosity, g is acceleration of gravity, k is thermal conductivity, h is enthalpy, and c_p is specific heat. S_{mass} is mass source terms, S_M is momentum source terms, and S_E is energy source terms.

In the arc model, Maxwell equations are employed to solve the electromagnetic field.

Current continuity

$$\nabla \cdot (\sigma_e \nabla \Phi) = 0 \quad (4)$$

Ohm's law

$$\mathbf{J} = -\sigma_e (\nabla \Phi) \quad (5)$$

Magnetic vector potential

$$\nabla^2 \mathbf{A} = -\mu_0 \mathbf{J} \quad (6)$$

Magnetic flux density

$$\mathbf{B} = \nabla \times \mathbf{A} \quad (7)$$

In the above equations, Φ is electric potential, σ_e is electric conductivity, \mathbf{J} is current density, μ_0 is permeability, \mathbf{A} is magnetic vector potential, and \mathbf{B} is magnetic flux density.

In present study, the arc model and metal transport model have the independent source terms.

2.1 Source terms of mass

In arc model, S_{mass} is equal to 0. In metal transfer model, the droplet is considered generating at a certain frequency and injecting to molten pool. Then the source term of mass can be written as,

$$S_{mass} = \frac{\rho_l}{\Delta t} \quad (8)$$

where ρ_l is density of liquid metal, Δt is droplet generation time.

The droplet is assumed to be a sphere. The initial diameter of droplet is determined by wire feeding rate, v_f , wire radius, R_w , and droplet transfer frequency, f_d [26]

$$D_d = \left(6R_w^2 \frac{\rho_w v_f}{\rho_d f_d} \right)^{1/3} \quad (9)$$

where ρ_w is density of wire and ρ_d is density of droplet.

2.2 Source terms of momentum

In arc model, the source term of momentum is electromagnetic force

$$S_M = \mathbf{J} \times \mathbf{B} \quad (10)$$

In metal transport model, the source terms of momentum can be written as

$$S_M = F_{mag} + F_b + F_{ms} \quad (11)$$

where F_{mag} is source terms of electromagnetic force which is obtained from the computational result of arc simulation and transmitted to metal transport model, F_b is buoyance which can be calculated by Boussinesq approximation

$$F_b = \rho\beta(T - T_{ref})g \quad (12)$$

, and F_{ms} is momentum source terms caused by solid-liquid mushy zone. The enthalpy-porosity technique is applied to treat the solid-liquid mushy zone as a porous medium with porosity equal to the liquid fraction. The liquid fraction is used to implicit track the solid-liquid interface. A momentum source, F_{ms} , is added to the momentum equation for representing the influence of mushy zone on flow

$$F_{ms} = \frac{(1 - \beta_l)^2}{(\beta_l^3 + \omega)} A_{mush} (\mathbf{V} - \mathbf{V}_p) \quad (13)$$

where β is thermal expansion coefficient, T is temperature, T_{ref} is reference temperature, A_{mush} is mushy zone constant, β_l is the liquid volume fraction, ω is a small number (0.001) to prevent division by zero and \mathbf{V}_p is the solid velocity due to the pulling of solidified material out of the domain.

2.3 Source terms of energy

In arc model, the source term of energy is given by

$$S_E = \frac{\mathbf{J} \cdot \mathbf{J}}{\sigma_e} + \frac{5k_b}{2e} \left(\frac{\mathbf{J}}{c_p} \cdot \nabla h \right) - S_R \quad (14)$$

where k_b is Boltzmann constant, e is elementary electric charge, S_R is radiation loss.

In metal transport model, the arc heat, S_{arc} , latent heat, S_L , and droplet heat, S_{drop} , are the source terms of weld pool (Eq. (15)). The S_{arc} is determined by internal energy boundary condition, and the S_L is defined by Eq. (16).

$$S_E = S_{arc} + S_L + S_{drop} \quad (15)$$

$$S_L = \frac{\Delta h}{c_p} \frac{\partial \beta_l}{\partial t} \quad (16)$$

The droplet heat, S_{drop} is considered by the droplet temperature. The initial temperature of droplet equals to 2100K [17, 18].

The deposition process and numerical model parameters [18] are shown in Table 1.

Table 1 Deposition process and numerical model parameters

Parameters	Value(unit)
Deposition current	200 A
Deposition voltage	26 V
Deposition speed	570 mm/min
Wire feeding rate	7.2 m/min
Shielding gas flow rate	15 L/min
Ambient temperature	300 K
Wire diameter	1.6 mm
Initial velocity of droplet	0.6 m/s

The physical properties of argon are temperature-dependent [14]. The substrate and wire are mild steel, and the thermophysical properties of mild steel are shown in Table 2 [18, 21, 22].

Table 2 Thermophysical properties of mild steel

Property	Value(unit)
Specific heat of solid phase	700 (J·kg ⁻¹ ·K ⁻¹)
Specific heat of liquid phase	780 (J·kg ⁻¹ ·K ⁻¹)
Thermal conductivity of solid phase	22 (W·m ⁻¹ ·K ⁻¹)
Thermal conductivity of liquid phase	22 (W·m ⁻¹ ·K ⁻¹)
Density of solid phase	7200 (kg·m ⁻³)
Density of liquid phase	7200 (kg·m ⁻³)
Dynamic viscosity	0.006 (kg·m ⁻¹ ·s ⁻¹)
Radiation emissivity	0.4
Heat convection coefficient	100 (W·m ⁻² ·K ⁻¹)
Latent heat of fusion	2.47e5(J·kg ⁻¹ ·K ⁻¹)
Solidus temperature	1750 K
Liquidus temperature	1800 K
Latent heat of vaporization	7.34e6 (J·kg ⁻¹ ·K ⁻¹)
Thermal expansion coefficient	4.95e-5 (K ⁻¹)
Permeability	1.26e-6(H·m ⁻¹)
Electric conductivity	7.7e5(m ⁻¹ ·W ⁻¹)
Surface tension coefficient	1.2 (N·m ⁻¹)
Surface tension temperature gradient	1e-4 (N·m ⁻¹ ·K ⁻¹)

3. Tracking of free surface

In present study, the VOF method is employed to track the free surface. A volume of fluid function, $F(x,y,z,t)$, is defined to indicate the topology of metal flow. This VOF function satisfies the following equation

$$\frac{dF}{dt} = \frac{\partial F}{\partial t} + (\mathbf{V} \cdot \nabla)F = 0 \quad (17)$$

According to the definition, a unit value corresponds to cells full of fluid (metal), while zero value corresponds to cells empty of fluid. Cells with F lies in 0 and 1 mean that the cells are located at the free surface. The gradient direction of F is the normal direction of free surface.

4. Boundary conditions

4.1 Internal boundary conditions

1) Internal momentum boundary conditions

In the arc model, the plasma shear stress acting on molten pool surface is determined by viscosity and velocity gradient of the arc plasma (Eq. (18)). And this surface force is added on metal surface (surface D in Fig. 5) as an internal boundary condition.

$$\tau_{ps} = \mu_{ps} \frac{\partial \mathbf{V}_{ps}}{\partial \mathbf{n}} \quad (18)$$

where μ_{ps} and \mathbf{V}_{ps} are the viscosity and velocity of plasma adjacent to metal surface.

In addition, the pressure on metal surface is determined by solving the momentum conservation equations in arc model.

In the metal transport model, the momentum boundary conditions of free surface (surface IJLK in Fig. 6) are plasma shear stress, arc pressure, surface tension and Marangoni shear stress, in which the plasma shear stress and arc pressure are obtained from the computational result of arc simulation and transmitted to metal transport model.

The surface tension of free surface can be written as

$$\tau_{st} = \gamma\kappa \quad (19)$$

$$\kappa = \nabla \cdot \frac{\nabla \varphi}{|\nabla \varphi|} \quad (20)$$

where γ is surface tension coefficient, κ is curvature of free surface. φ is the shape function of free surface defined by the volume fraction F .

Marangoni shear stress tangential to the metal free surface is given by

$$\tau_{ma} = \frac{\partial \gamma}{\partial T} \frac{\partial T}{\partial \mathbf{n}} \quad (21)$$

All the surface forces on free surface are transformed to localized body forces and added to the momentum equations as source terms^[21, 22].

2) Internal energy boundary conditions

In the arc model, the net heat flux of metal surface (surface D in Fig. 5) can be expressed by^[21, 23, 25]

$$q_{net} = K_{eff} \frac{T_{p,c} - T_c}{\delta} - \varepsilon k_b T_c^4 - q_{ev} H_{ev} \quad (22)$$

$$\log(q_{ev}) = 2.52 + (6.21 - \frac{18836}{T_c}) - 0.5 \log(T_c) \quad (23)$$

where K_{eff} represents the effective thermal conductivity and δ is thickness of sheath, ε is radiation emissivity. $T_{p,c}$ is the plasma temperature adjacent to cathode metal, T_c is cathode temperature. H_{ev} is the latent heat for liquid-vapor phase-change, q_{ev} is the melt mass evaporation rate. The terms on the right-hand side of Eq. (22) are the contribution due to thermal conduction from the arc to metal, the radiation loss and the heat loss due to the evaporation of metal, respectively.

In the metal transport model, the net heat flux on molten pool free surface is determined by arc simulation, and transmitted to metal transport model by UDS. And this heat flux boundary condition of metal transport model is also applied on surface IJLK (free surface of molten pool) in Fig. 6.

The all internal boundary conditions of arc model are listed in Table 3. The ‘Coupled’ in Fluent means the coupling between the metal and arc which is to ensure the continuity of electric current and magnetic potential at the interface.

Table 3 The internal boundary conditions of arc model

Boundary	$\mathbf{V}(\text{m}\cdot\text{s}^{-1})$	$p(\text{Pa})$	$T(\text{K})$	$\Phi(\text{V})$	$\mathbf{A}(\text{Wb}\cdot\text{s}^{-1})$
B	--	--	1000	Coupled	Coupled
C	--	--	3000	Coupled	Coupled
D	--	--	Eq. (22)	Coupled	Coupled

4.2 External boundary conditions of computational domain

The external boundary conditions of arc models are listed in Table 4.

Table 4 The external boundary conditions of arc model

Boundary	$\mathbf{V}(\text{m}\cdot\text{s}^{-1})$	$p(\text{Pa})$	$T(\text{K})$	$\Phi(\text{V})$	$\mathbf{A}(\text{Wb}\cdot\text{s}^{-1})$
A	--	--	1000	$-\sigma_e \frac{\partial \Phi}{\partial z} = \frac{I_w}{\pi R_w^2}$	$\partial A / \partial n = 0$

E	--	--	Eq. (24)	0	$\partial A / \partial n = 0$
F	Eq. (25)	101325	1000	$\partial \Phi / \partial n = 0$	$\partial A / \partial n = 0$
G	--	101325	$\partial T / \partial n = 0$	$\partial \Phi / \partial n = 0$	$A = 0$
H	--	--	$\partial T / \partial n = 0$	$\partial \Phi / \partial n = 0$	$A = 0$

The convection and radiation boundary conditions are used to describe heat loss of external boundary^[35]

$$-k \frac{\partial T}{\partial \mathbf{n}} = h_{conv} (T - T_{amb}) + \varepsilon k_b (T^4 - T_{amb}^4) \quad (24)$$

where Q is gas flow rate, R_w is wire radius and R_n is nozzle inner radius.

The velocity of shielding gas inlet can be written as^[23]

$$v_z(r) = \frac{2Q}{\pi} \frac{\left\{ R_n^2 - r^2 + (R_n^2 - R_w^2) \frac{\ln(r/R_n)}{\ln(R_n/R_w)} \right\}}{\left\{ R_n^4 - R_w^4 + \frac{(R_n^2 - R_w^2)^2}{\ln(R_n/R_w)} \right\}}, \quad r = \sqrt{x^2 + y^2}, r \in [R_w, R_n] \quad (25)$$

The external boundary conditions of metal transport models are listed in Table 5.

Table 5 The external boundary conditions of metal transport model

Boundary	V(m/s)	T(K)	p(Pa)
IJCD	--	Eq. (24)	--
ICGK	--	Eq. (24)	--
KLHG	--	Eq. (24)	--
JDLH	--	Eq. (24)	--
ABJI	--	$\partial T / \partial n = 0$	101325
AIKE	--	$\partial T / \partial n = 0$	101325
EFLK	--	$\partial T / \partial n = 0$	101325
FBJL	--	$\partial T / \partial n = 0$	101325
ABFE	Eq. (25)	1000	101325
CDHG	--	Eq. (24)	--

Numerical considerations

1. Coupling methods of the arc and metal transport model

The molten pool is simplified to be solid state on the basis of experimental results and the arc is simulated firstly. Then the electromagnetic force, plasma shear stress, arc pressure and net heat flux are transmitted to metal transport model. In the Fluent, the result variables can be written in user-defined scalars (UDSs) and exported as files. These files can be imported in another model by the way of interpolation. Therefore, the interpolation function of UDS is used to do the transmissions, and this interpolation function is capable of adapting different grids under the same coordinate system.

In metal transport model, the electromagnetic force can be added to the momentum conservation equations as a source term directly by UDS. The plasma shear stress, Marangoni shear stress, arc pressure and surface tension act on molten pool surface. Therefore, a continuum surface forces (CSF) method is applied to transform all the surface forces to localized body forces. And then these localized body forces are added to the momentum conservation equations as source terms at boundary cells [10, 12, 14].

$$F_{vol} = \tau_{SF} \frac{\rho \nabla F}{\frac{1}{2}(\rho_1 + \rho_2)} \quad (26)$$

where ∇F is VOF gradient, ρ_1 and ρ_2 are the density of first and second phases, respectively. τ_{SF} represents the surface forces on free surface.

The net heat flux is also accounted for by adding source term to the energy conservation equation at the interface layer cells [29].

2. Initialization

The moving electrode is not considered in this study. Therefore the initial morphologies of weld bead and molten pool are initialized in the same way as the arc simulation in metal transport model (as shown in Fig. 6). To reproduce the actual shape of molten pool, a double ellipsoid temperature field is used to initialize the temperature field of molten pool, the formula of this initial temperature field is expressed as

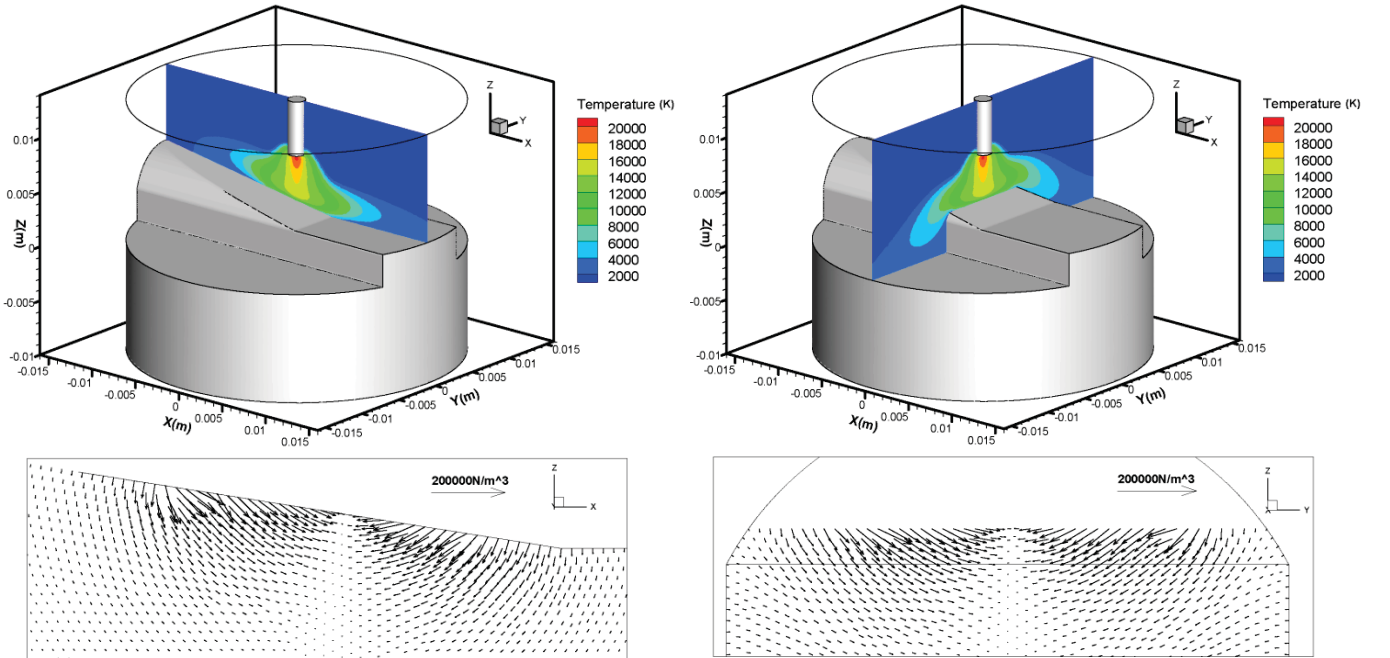
$$T_0(x, y, z) = \begin{cases} T_{center} \exp\left(\frac{-3x^2}{a_r^2}\right) \exp\left(\frac{-3y^2}{b^2}\right) \exp\left(\frac{-3z^2}{c^2}\right), x < 0 \\ T_{center} \exp\left(\frac{-3x^2}{a_f^2}\right) \exp\left(\frac{-3y^2}{b^2}\right) \exp\left(\frac{-3z^2}{c^2}\right), x \geq 0 \end{cases} \quad (27)$$

where T_{center} is the center temperature, a_r and a_f are rear and front ellipsoid radius, b is ellipsoid width, c is ellipsoid radius of depth direction.

Results and discussions

1. Results of arc simulation

Fig. 7 shows the simulated results of arc temperature and molten pool electromagnetic force at XZ plane ($Y=0$) and YZ plane ($X=0$). It can be seen from Fig. 7 that the temperature field and molten pool electromagnetic force are asymmetric distribution at XZ plane, but symmetric distribution at YZ plane.



(a) (b)
 Fig. 7 Simulated results of arc temperature and molten pool electromagnetic force: (a) XZ plane; (b) YZ plane

Fig. 8 displays the arc profile captured by high-speed camera. After the comparison of Fig.7 (b), it can be found that the arc profile of simulation and captured by high-speed camera are in good agreement.

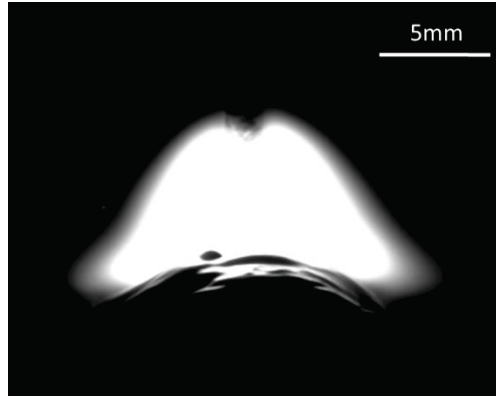


Fig.8 Arc profiles are captured by high-speed camera

Fig. 9 exhibits the paths on the surface of deposited layer. Fig. 10 shows the distributions on Path x and Path y. The curves labeled ‘-emfx’, ‘-emfy’, ‘-hx’, ‘-hy’, ‘-px’, ‘-py’, ‘-plax’ and ‘-play’ represent the electromagnetic force, net heat flux, pressure and plasma shear stress on Path x and Path y, respectively. It can be seen from Fig. 10 that all the distributions on Path y are symmetric distribution due to the symmetric morphology of deposited layer. The electromagnetic force and pressure deviate to the rear of molten pool on Path x, and the peak value of electromagnetic force also locates at the rear of molten pool. The centers of pressure distribution on Path x and Path y show a small deviation. The peak value of net heat flux and plasma shear stress are deviate to the front of molten pool on Path x.

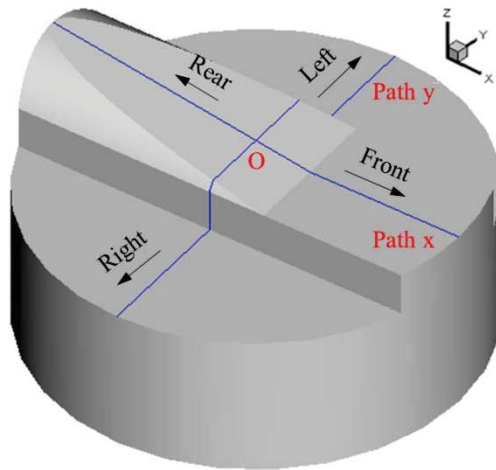


Fig.9 Schematic diagram of paths on surface of deposition layer

Fig. 10 also demonstrate that because of the asymmetrical deposited layer morphology, the electromagnetic force, net heat flux, pressure and plasma shear stress on the surface of molten pool are not completely symmetrical confirming that the morphology of the deposited layers has important influence on these distributions. In the conventional separated model, the effects of topography of deposited layers on the distributions are usually neglected. Apparently, these asymmetric distributions can't be neglected in AWAM

deposition. Compared with the symmetrical empirical model of electromagnetic force and pressure [16,17], this modeling method is more realistic and has higher accuracy.

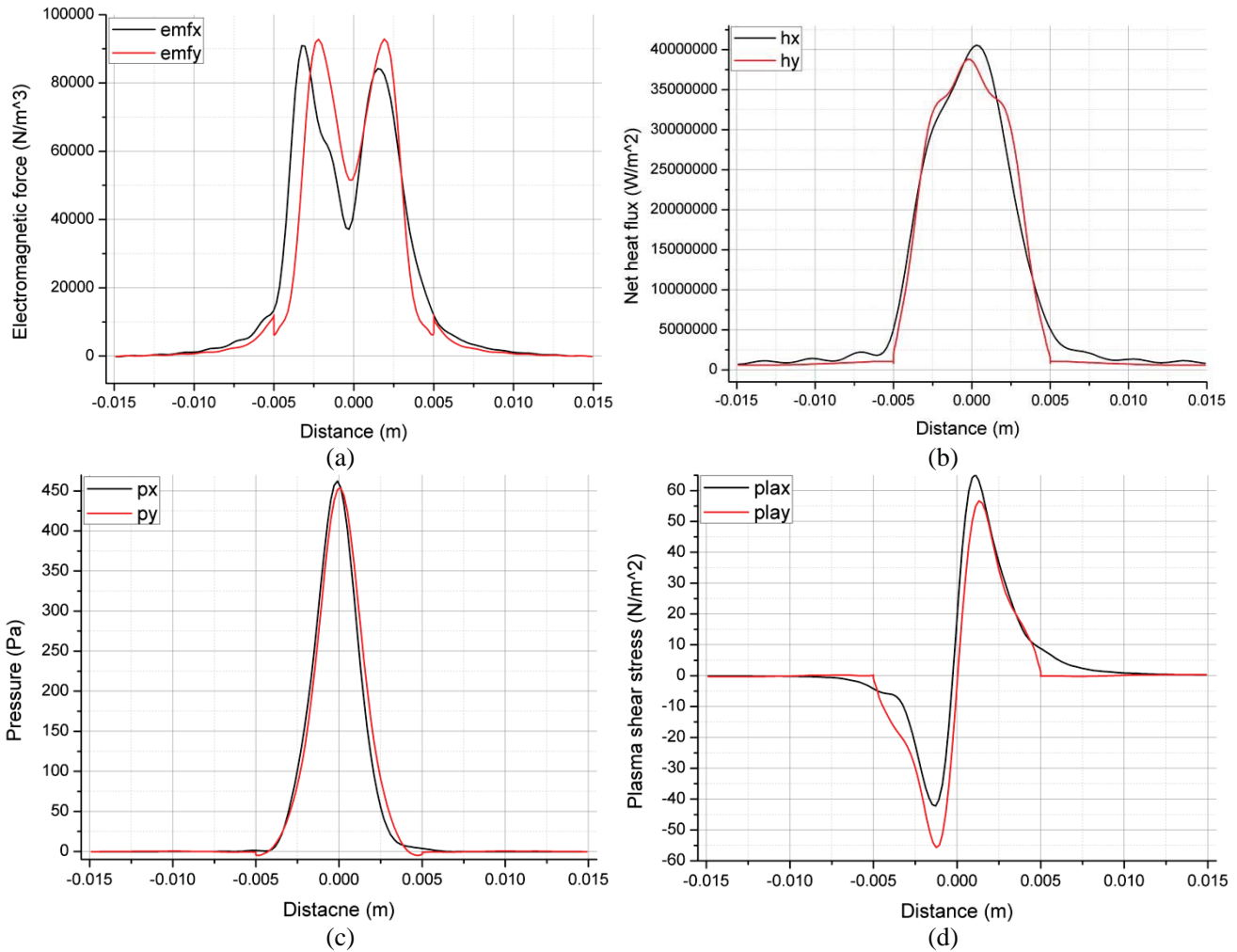
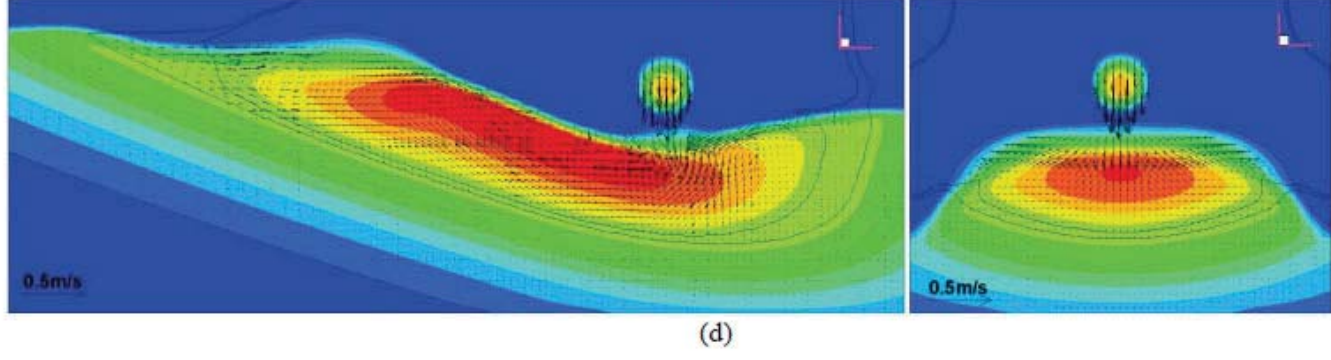
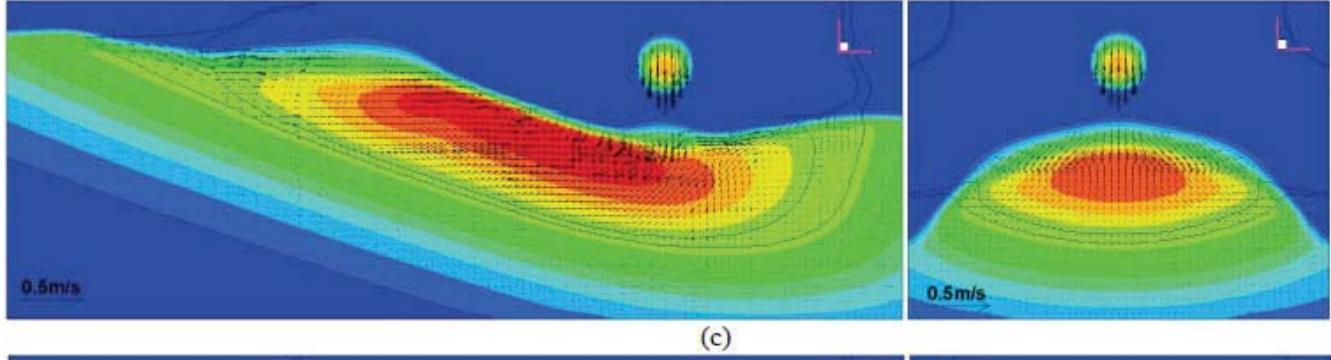
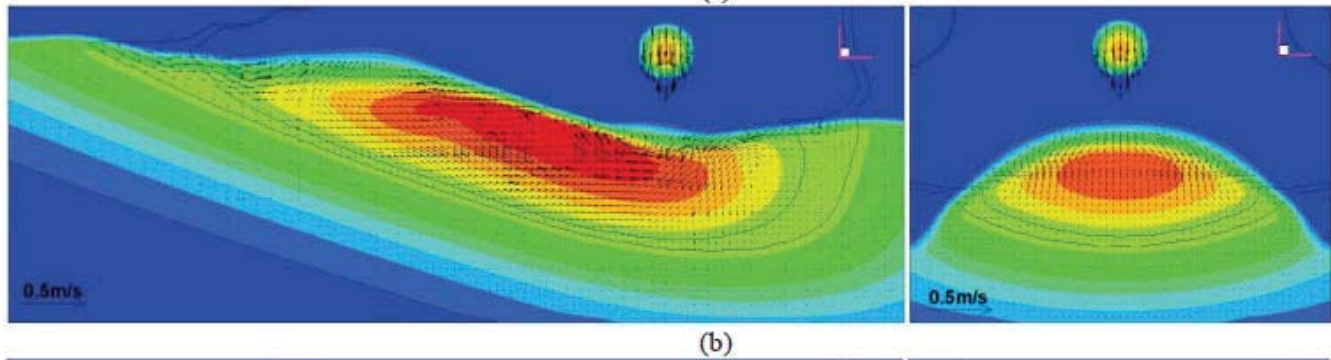
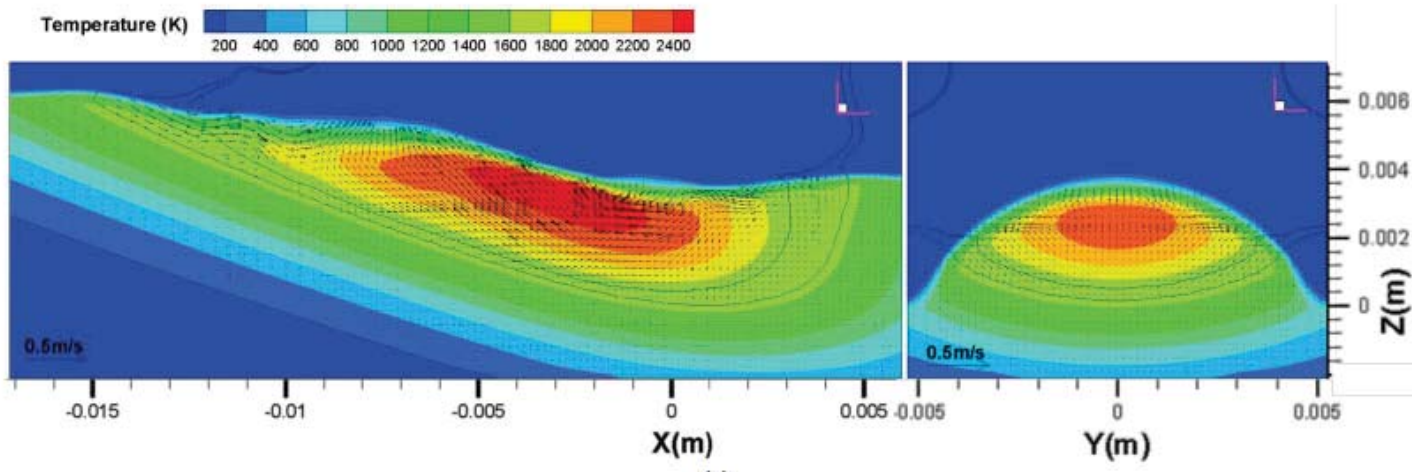


Fig.10 Distributions on path x and path y: (a) electromagnetic force; (b) net heat flux; (c) pressure; (d) plasma shear stress.

2. Results of metal transport simulation

Fig. 11 displays the temperature and velocity vector distribution of molten pool at different instants. The temperature and velocity of molten pool distribute symmetrically at YZ plane ($X=0$). Due to the downward electromagnetic force and positive surface tension temperature gradient, the metal in the center of molten pool flow to the bottom and back of molten pool, which result in the high temperature region of molten pool deviates to rear of molten pool. The droplet impingement (as shown in Fig. 11(b~f)) brings the heat input and results in increasing temperature and oscillation of molten pool. In addition, this impingement and back flow metal drive molten metal flow to rear of molten pool (as shown in Fig. 11(e~g)). In a continuous deposition process, these metal transport phenomena will form the final morphology of weld bead and periodic arc-shaped ripples on solidified weld bead [17].



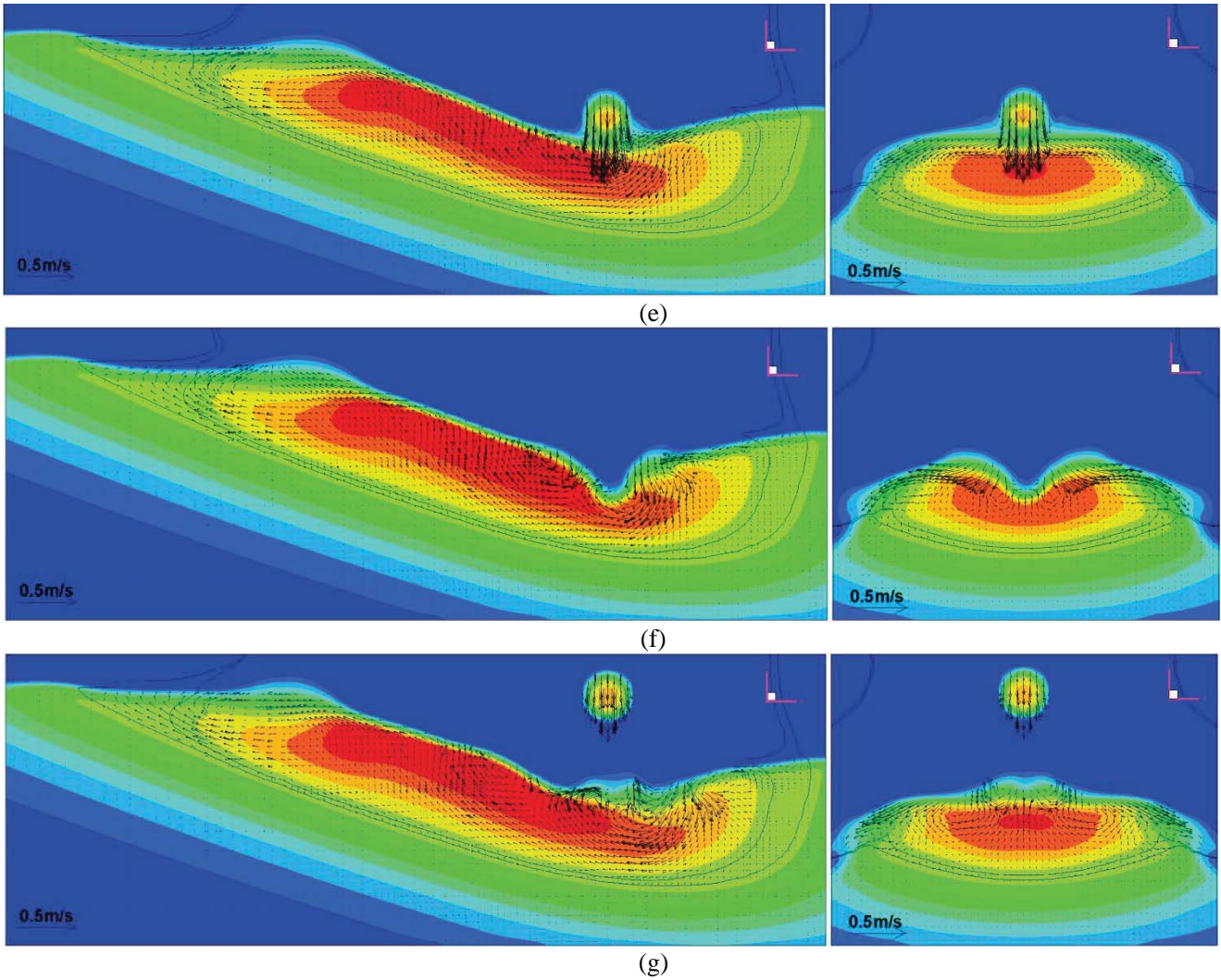


Fig.11 The temperature and velocity vector distribution at different instants: (a) 0.020s; (b) 0.024s (c) 0.028s; (d) 0.032s; (e) 0.036s; (f) 0.040s; (f) 0.044s.

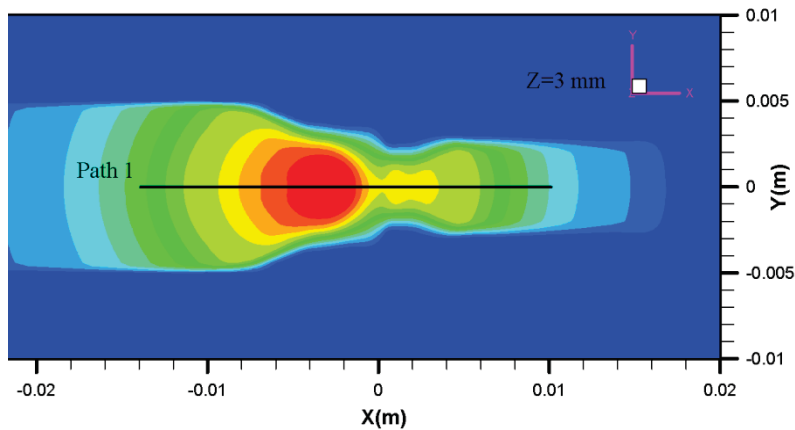


Fig. 12 Schematic diagram of path 1 on $Z = 3$ mm plane.

Fig. 12 shows the schematic diagram of path 1 on the plane at $Z = 3$ mm, namely the plane locates at the top surface of first layer. Fig.13 represents the temperature and velocity magnitude distributions on path 1 at different instants. It can be seen clearly from Fig. 13(a) that the peak temperature on Path 1

increases with time. Due to the droplet impingement and arc heat input, the peak temperature increase to 2560 K at 0.044s. Additionally, the temperature distribution between the -0.0025m to 0.005m on Path 1 appears oscillation due to the droplet impingement and molten pool oscillation. From Fig. 13(b), it can be seen that the velocity magnitude on Path 1 reaches its maximum value at 0.036s, but the position of the maximum velocity deviates from the center of molten pool. Subsequently, the velocity decreases obviously due to the impact energy absorbed by the molten pool oscillation.

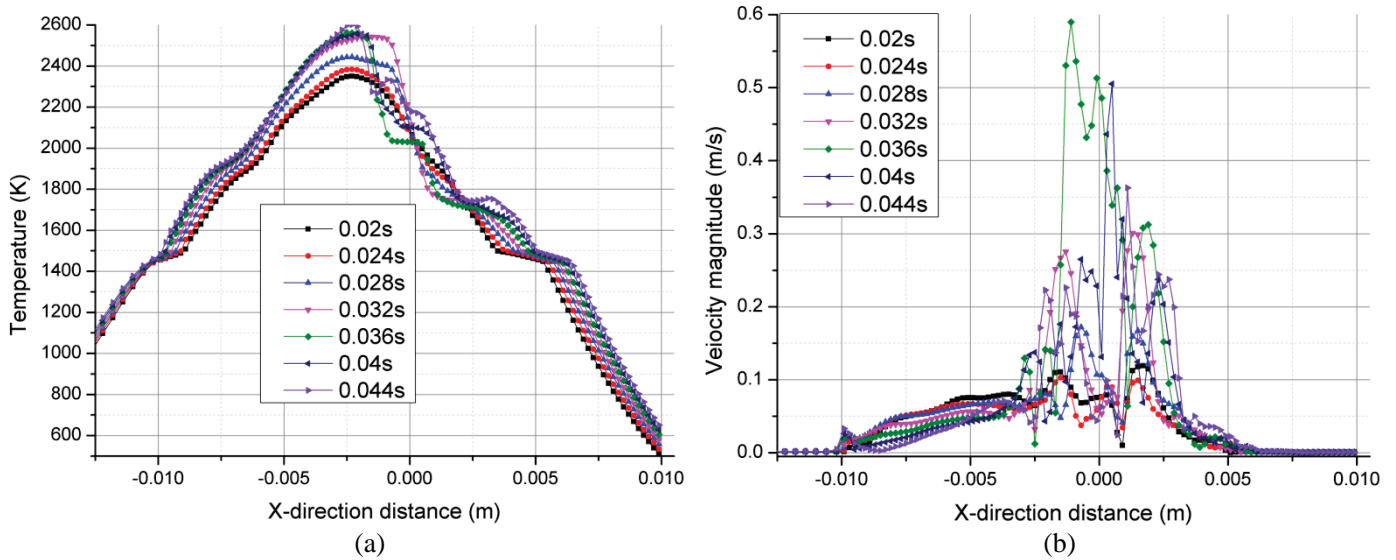


Fig. 13 Distributions on path 1 at different instants: (a) temperature; (b) velocity magnitude.

Fig. 14 displays the comparison of molten pool morphology between the simulated and experimental result. It can be seen from Fig. 14 that the molten pool morphology of simulated and experimental result is in good agreement. In addition, because only the molten pool rather than whole deposition process was simulated, there had no periodic arc-shaped ripples forming on weld bead surface in simulated result.

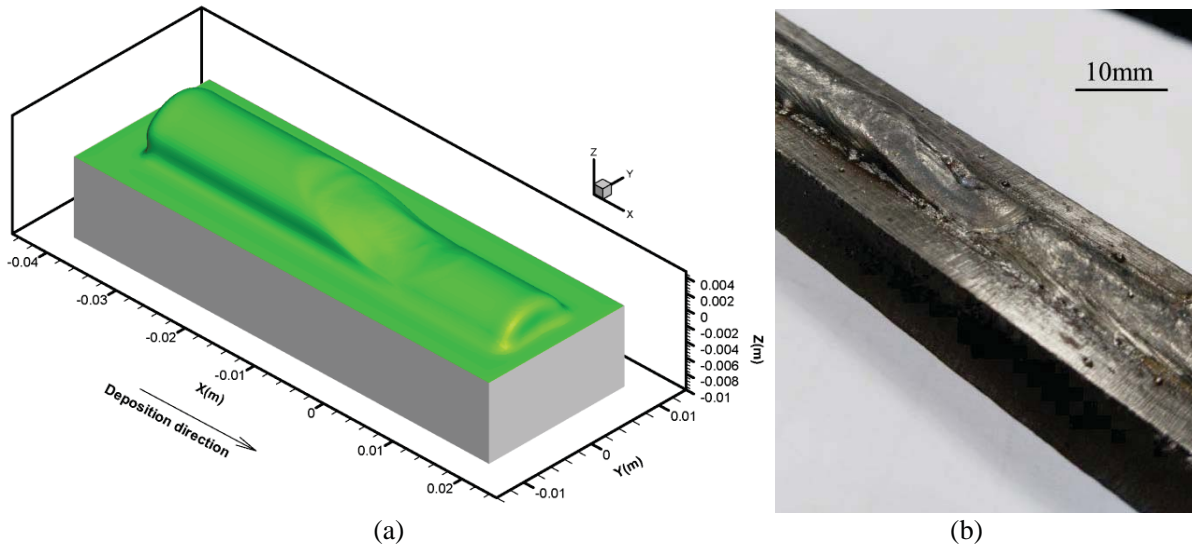


Fig. 14 The molten pool morphology: (a) simulated result; (b) experimental result.

Conclusions

A three-dimensional weak coupling modeling method of arc and metal transport has been developed to simulate the arc and metal transport of stacking deposition in GMAW based additive manufacturing. The following main conclusions are gained:

(1) The evolvments of the distribution on surface of deposited layer show that the electromagnetic force and net heat flux are not completely symmetrical distribution.

(2) The high temperature region in molten pool deviates to the rear of molten pool. The droplet impingement brings the heat input and results in increasing temperature and oscillation of molten pool. And this impingement and back flow metal drive molten metal flowing to the rear of molten pool.

(3) The simulated result of the molten pool morphology accords well with experimental result of stacking deposition, which shows that this weak coupling modeling method is capable of simulating the complex heat and mass transfer phenomena in arc welding based additive manufacturing.

References

- [1] Sing S L, Yeong W Y, Wiria F E. [Selective laser melting of titanium alloy with 50 wt% tantalum: Microstructure and mechanical properties. *Journal of Alloys and Compounds*, 2016,660:461-470.
- [2] Liu J, Gao C, Feng P, et al. Selective laser sintering of β -TCP/nano-58S composite scaffolds with improved mechanical properties. *Materials & Design*, 2015,84(9):395-401.
- [3] Hinojos A, Mireles J, Reichardt A, et al. Joining of Inconel 718 and 316 Stainless Steel using electron beam melting additive manufacturing technology. *Materials & Design*, 2016,94:17-27.
- [4] Yan W, Yue Z, Zhang J. Study on the residual stress and warping of stiffened panel produced by electron beam freeform fabrication. *Materials & Design*, 2016,89:1205-1212.
- [5] Gu J, Ding J, Williams S W, et al. The strengthening effect of inter-layer cold working and post-deposition heat treatment on the additively manufactured Al - 6.3Cu alloy. *Materials Science and Engineering: A*, 2016,651:18-26.
- [6] Zhang H, Wang X, Wang G, et al. Hybrid direct manufacturing method of metallic parts using deposition and micro continuous rolling. *Rapid Prototyping Journal*, 2013,19(6):387-394.
- [7] Ding D, Pan Z, Cuiuri D, et al. Bead modelling and implementation of adaptive MAT path in wire and arc additive manufacturing. *Robotics and Computer-Integrated Manufacturing*, 2016,39:32-42.
- [8] Xiong J, Zhang G, Zhang W. Forming appearance analysis in multi-layer single-pass GMAW-based additive manufacturing. *The International Journal of Advanced Manufacturing Technology*, 2015,80(9-12):1767-1776.
- [9] Ding J, Colegrove P, Mehnen J, et al. Thermo-mechanical analysis of Wire and Arc Additive Layer Manufacturing process on large multi-layer parts. *Computational Materials Science*, 2011.
- [10] Ding D, Pan Z, Cuiuri D, et al. A multi-bead overlapping model for robotic wire and arc additive manufacturing (WAAM). *Robotics and Computer-Integrated Manufacturing*, 2015,31:101-110.
- [11] XU G, HU J, TSAI H. L. Modeling Three-Dimensional Plasma Arc in Gas Tungsten Arc Welding. *Journal of Manufacturing Science & Engineering*, 2012, 134(3):40-80.
- [12] Haidar J. The dynamic effects of metal vapour in gas metal arc welding. *Journal of Physics D: Applied Physics*, 2010,43(16):165204.
- [13] Xueping D, Huan L, Huiliang W, et al. Numerical analysis of arc plasma behavior in double-wire GMAW. *Vacuum*, 2016,124:46-54.
- [14] Zhou X M, Zhang H O, Wang G L, et al. Simulation of the influences of surface topography of deposited layer on arc shape and state in arc based additive forming. *Acta Physica Sinica*, 2016, 65(3).
- [15] Wu C S, Chen J, Zhang Y M. Numerical analysis of both front- and back-side deformation of fully-penetrated GTAW weld pool surfaces. *Computational Materials Science*, 2007,39(3):635-642.
- [16] Chen J, Schwenk C, Wu C S, et al. Predicting the influence of groove angle on heat transfer and fluid flow for new gas metal arc welding processes. *International Journal of Heat & Mass Transfer*, 2012, 55(1-3):102-111..
- [17] Hu J, Guo H, Tsai H L. Weld pool dynamics and the formation of ripples in 3D gas metal arc welding. *International Journal of Heat and Mass Transfer*, 2008,51(9-10):2537-2552.
- [18] Rao Z H, Zhou J, Liao S M, et al. Three-dimensional modeling of transport phenomena and their effect on the formation

- of ripples in gas metal arc welding. *Journal of Applied Physics*, 2010,107(5):54905.
- [19] Cho D, Song W, Cho M, et al. Analysis of submerged arc welding process by three-dimensional computational fluid dynamics simulations. *Journal of Materials Processing Technology*, 2013,213(12):2278-2291.
- [20] Cho D, Na S. Molten pool behaviors for second pass V-groove GMAW. *International Journal of Heat and Mass Transfer*, 2015,88:945-956.
- [21] Hu J, Tsai H L. Heat and mass transfer in gas metal arc welding. Part I: The arc. *International Journal of Heat and Mass Transfer*, 2007,50(5-6):833-846.
- [22] Hu J, Tsai H L. Heat and mass transfer in gas metal arc welding. Part II: The metal. *International Journal of Heat and Mass Transfer*, 2007,50(5-6):808-820.
- [23] Rao Z H, Hu J, Liao S M, et al. Modeling of the transport phenomena in GMAW using argon - helium mixtures. Part I - The arc. *International Journal of Heat and Mass Transfer*, 2010,53(25-26):5707-5721.
- [24] Rao Z H, Hu J, Liao S M, et al. Modeling of the transport phenomena in GMAW using argon - helium mixtures. Part II - The metal. *International Journal of Heat and Mass Transfer*, 2010,53(25-26):5722-5732.
- [25] Murphy A B. A self-consistent three-dimensional model of the arc, electrode and weld pool in gas - metal arc welding. *Journal of Physics D: Applied Physics*, 2011,44(19):194009.
- [26] Murphy A B. Influence of droplets in gas - metal arc welding: new modelling approach, and application to welding of aluminium. *Science and Technology of Welding and Joining*, 2013,18(1):32-37.
- [27] Wang X, Fan D, , et al. A unified model of coupled arc plasma and weld pool for double electrodes TIG welding. *Journal of Physics D: Applied Physics*, 2014,47:14.
- [28] Wang X, Fan D, , et al. Numerical simulation of arc plasma and weld pool in double electrodes tungsten inert gas welding. *International Journal of Heat and Mass Transfer*, 2015,85:924-934.
- [29] Jian X, Wu C S. Numerical analysis of the coupled arc - weld pool - keyhole behaviors in stationary plasma arc welding. *International Journal of Heat and Mass Transfer*, 2015,84:839-847.
- [30] Xu G, Hu J, Tsai H L. Three-dimensional modeling of arc plasma and metal transfer in gas metal arc welding. *International Journal of Heat and Mass Transfer*, 2009,52(7-8):1709-1724.
- [31] Xiong J, Zhang G, Gao H, et al. Modeling of bead section profile and overlapping beads with experimental validation for robotic GMAW-based rapid manufacturing. *Robotics and Computer-Integrated Manufacturing*, 2013,29(2):417-423.
- [32] Hsu K C P E. Two - temperature modeling of the free - burning, high - intensity arc. *Journal of Applied Physics*, 1983,8(54):4359-4366.
- [33] Xu G, Hu J, Tsai H L. Three-dimensional modeling of the plasma arc in arc welding. *Journal of Applied Physics*, 2008,104(10):103301.
- [34] Hsu K C, Etemadi K, Pfender E. Study of the free-burning high-intensity argon arc. *Journal of Applied Physics*, 1983,54(3):1293.
- [35] Bai X, Zhang H, Wang G. Modeling of the moving induction heating used as secondary heat source in weld-based additive manufacturing. *The International Journal of Advanced Manufacturing Technology*, 2015,77(1-4):717-727.